

ARTICLE

Received 25 Feb 2015 | Accepted 22 Jun 2015 | Published 5 Aug 2015

DOI: 10.1038/ncomms8872

OPEN

High-rate aluminium yolk-shell nanoparticle anode for Li-ion battery with long cycle life and ultrahigh capacity

Sa Li^{1,2,*}, Junjie Niu^{2,3,*}, Yu Cheng Zhao¹, Kang Pyo So², Chao Wang², Chang An Wang¹ & Ju Li^{2,4}

Alloy-type anodes such as silicon and tin are gaining popularity in rechargeable Li-ion batteries, but their rate/cycling capabilities should be improved. Here by making yolk-shell nanocomposite of aluminium core (30 nm in diameter) and TiO₂ shell (~3 nm in thickness), with a tunable interspace, we achieve 10 C charge/discharge rate with reversible capacity exceeding 650 mAh g⁻¹ after 500 cycles, with a 3 mg cm⁻² loading. At 1 C, the capacity is approximately 1,200 mAh g⁻¹ after 500 cycles. Our one-pot synthesis route is simple and industrially scalable. This result may reverse the lagging status of aluminium among high-theoretical-capacity anodes.

¹State Key Lab of New Ceramics and Fine Processing, School of Materials Science and Engineering, Tsinghua University, Beijing 100084, P. R. China.

²Department of Nuclear Science and Engineering, Massachusetts Institute of Technology, Cambridge, Massachusetts 02139, USA. ³Department of Materials Science and Engineering, University of Wisconsin-Milwaukee, Milwaukee, Wisconsin 53211, USA. ⁴Department of Materials Science and Engineering, Massachusetts Institute of Technology, Cambridge, Massachusetts 02139, USA. * These authors contributed equally to this work. Correspondence and requests for materials should be addressed to C.A.W. (email: wangca@mail.tsinghua.edu.cn) or to J.L. (email: liju@mit.edu).

Aluminium should be an attractive anode material for rechargeable Li-ion batteries for many reasons, such as low cost ($\sim \$2,000 \text{ ton}^{-1}$), high theoretical capacity ($2,235 \text{ mAh g}^{-1}$ if Li_9Al_4 (refs 1,2)), low potential plateau ($\sim 0.19\text{--}0.45 \text{ V}$ against Li^+/Li^3), high electrical conductivity and so on. However, despite the historical efforts on developing Al-Li electrodes, the practical performance fell far short of the theoretical promise and many other high-capacity anodes³. The best result so far came from Park *et al.*,⁴ whose hybridized 40 wt % Al/C₆₀ anode showed a capacity of $>900 \text{ mAh g}^{-1}$ over 100 cycles. Most of the batteries using aluminium films of micron thickness displayed a high initial capacity, but faded rapidly in a few cycles. Fundamentally this is because of two damage mechanisms, both exacerbated by aluminium's $\sim 100\%$ volume expansion/shrinkage during lithiation/delithiation: (a) the volume changes cause repeated breaking and re-formation of the solid-electrolyte interphase (SEI) film coating the active material^{3,6}, making Coulombic efficiency (CE) $\neq 100\%$ in a cycle and converting cycleable or 'live' lithium in the electrodes and electrolyte to 'dead lithium' in SEI, and eventually the battery dies out of lithium exhaustion, and (b) the active material (Al-Li) could pulverize or be pushed away during cycling, thus losing electrical contact from the current collector.

The above are actually generic problems for all high-capacity anode materials^{1,7,8}. Many pioneering works have shown that a predefined void space and/or a conductive buffer can counteract failure mechanisms (a) and (b)^{9–11}. Cui *et al.*, demonstrated that creating yolk-shell nanoarchitectures^{12,13} could be a very effective solution, as an inert nanoshell facing the electrolyte is covered with SEI but does not change volume, while the active yolk expands/shrinks in the internal cavity without SEI. Also, because the thin carbon shell conducts both Li^+ and electron¹⁴, even if the yolk pulverizes, the active contents are still confined in the closed shell and will not lose electrical contact. Ultrahigh capacity and long cycle life have been realized in the Si yolk-carbon shell electrode^{7,12}. We believe this general paradigm should also work for aluminium active core. The key practical question is how to generate fully closed TiO_2 nanoshell¹⁴ around aluminium nanoparticles with tunable vacuum interspace in between (Al@ TiO_2) in a cost-effective and industrially scalable way. From materials design point of view, the Al@ TiO_2 yolk-shell nanostructure must satisfy the following requirements: (A) The shell must be thin enough, as size-dependent transport¹⁴ makes thicker TiO_2 shell a much poorer electron and Li^+ conductor¹⁵. Modelling shows that sub-10 nm TiO_2 shell has definite advantage over thicker TiO_2 shells in transport¹⁴. And since TiO_2 has a much lower capability of lithium storage than aluminium, thinner shells mean higher specific capacity of TiO_2 -nanoaluminum hybrid. Practically we are talking about TiO_2 shell thickness $h \leq 5 \text{ nm}$ for effective transport. (B) The shell must be mechanically robust, as internal stress will still be generated within one yolk-shell due to adhesion between Al-Li core and TiO_2 shell during lithiation/delithiation, and we do not want the thin shell to fracture in tension. Requirement (A) appears to be opposite to requirement (B), because too thin h clearly cannot sustain tensile load without rupturing, and too thick h works against transport requirement (A). But coming to the rescue, there is strong evidence that nanoscale oxides have fundamentally different mechanical behaviour from its macroscale counterpart^{16,17}, and can be surprisingly robust mechanically^{8,18,19}. So h of a few nanometres appears to work well enough to satisfy both (A) and (B) requirements. (C) The shell must be fully closed. This is because otherwise the liquid electrolyte can get into the void interspace by convection and generate SEI directly on aluminium surface, which triggers failure mode (a). Also, if the yolk pulverizes and the shell is not closed,

the active content can spill into the electrolyte, triggering failure mode (b). (D) There must be sufficient void spacing between the yolk and shell. Since volume expansion of aluminium is $\sim 96\%$, the shell-enclosed volume ($\pi D^3/6$, where D is the inner diameter of the TiO_2 shell) must be at least double that of the aluminium nanoparticle ($\pi d_0^3/6$, where d_0 is the diameter of the aluminium yolk before lithiation). Practically:

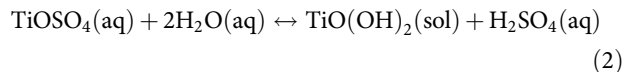
$$\pi D^3/6 = \pi d_0^3/6 \times B \quad (1)$$

where we find the optimal fill factor B to be 2.5–4. Still larger B would reduce the volumetric specific capacity of Al@ TiO_2 and increase the diffusion distance, which would lead to a larger overpotential and poorer rate performance of the electrodes²⁰.

In this work we report a one-pot synthesis method that is simple, cheap, scalable and uses only Earth-abundant elements (Al, Ti, O, H, C and S) and therefore can be used for mass production. The method gives specific capacities (defined based on the total weight of Al@ TiO_2 nanocomposite, or ATO powder) shown in the Abstract at an industrially sensible loading of $3 \text{ mg Al@TiO}_2 \text{ cm}^{-2}$ on copper foil. The synthesis method is derived somewhat serendipitously. It started from the observation that some commercial aluminium powders come with a relatively thick adherent surface oxide layer of Al_2O_3 (alumina). Even though an ultrathin alumina membrane (by atomic-layer deposition) on high-capacity anodes could enhance performance^{19,21}, such a thick layer of natural alumina worsens battery performance and needs to be removed. However, even if some chemical methods could be utilized to eliminate the natural alumina layer, in air, the fresh aluminium will be oxidized again very quickly. It would be great if we can design a wet-chemical environment in which the thick, adherent natural alumina layer can be converted to the beneficial, non-adherent TiO_2 shell envisioned in (A)–(D) in just one step, to create the Al@ TiO_2 yolk-shell structure (ATO) for air-stable and long-cycle-life anode. In other words, in one stroke we would like to convert the 'bad' oxide (thick adherent alumina) to the 'good' oxide (partially detached TiO_2 shell). By making yolk-shell nanocomposite of aluminium core and TiO_2 shell, with a tunable interspace, we achieve 10 C charge/discharge rate with reversible capacity exceeding 650 mAh g^{-1} after 500 cycles. At 1 C, the capacity is around $1,200 \text{ mAh g}^{-1}$ after 500 cycles.

Results

Preparation of Al@ TiO_2 yolk-shell nanoparticles. The chemistry for the 'wet conversion' has been found, which is water-based sulfuric acid ($[\text{H}^+] = 1 \text{ M}$) saturated with titanium oxysulfate (TiOSO_4), where the concentration of TiOSO_4 (aq) is at the solubility limit of solid $\text{TiO}(\text{OH})_2$ that sat at the bottom of the acid bath and later filtered out:



The schematic is shown in Fig. 1a. Then, we simply place commercial aluminium powder (diameter $D_0 \sim 50 \text{ nm}$), which have a surface layer of natural alumina, into the acid. The following 'water-shift' reactions (3) and (4) then take place:



where alumina is converted into aluminium sulfate (soluble) that diffuses away, and extra water. The extra water then shifts the thermodynamic balance of (2) to its right-hand side



and precipitates out solid $\text{TiO}(\text{OH})_2$ nanoshell *in situ*, by nucleation and growth at the original diameter D_0 . Since alumina is being consumed and the original particle recedes, the

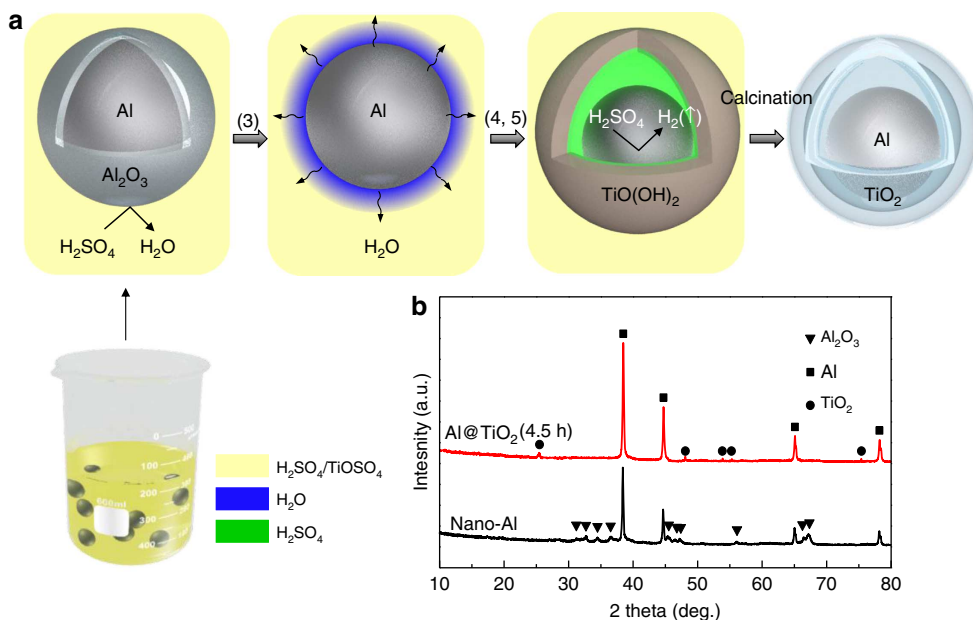
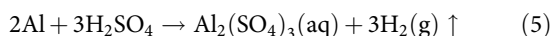


Figure 1 | Synthesis and characterization of Al@TiO₂. (a) Schematic of the ‘in situ water-shift’ synthesis of Al@TiO₂. The colours represent chemical contents in the solution: the equilibrated mixture of H₂SO₄ and TiOSO₄ is light yellow, H₂O is blue, and H₂SO₄ is green. (b) X-ray diffraction data of commercial nano aluminium powder and the as-obtained Al@TiO₂ with 4.5 h etching. The original Al₂O₃ layer is completely eliminated after our experimental procedure and the final product consists of pure metallic aluminum and anatase.

TiO(OH)₂ solid shell at D_0 starts to detach from the original particle at this point. Once alumina is completely consumed, reaction (5) takes place:



which further separates the yolk and the shell, and the interspace grows. Experimentally, we discovered reaction (5) happens slowly, on the timescale of hours. This slow etching of aluminium nanocore when there is plenty of acid in the solution proves that by the time Al₂O₃ is gone, the TiO(OH)₂ shell is already fully enclosed and semi-protective, preventing the bulk acid from flowing inside by convection. But the solid TiO(OH)₂ still allows H⁺, SO₄²⁻, Al³⁺ ions to exchange through the shell, probably through grain boundary diffusion. So a grain boundary diffusion controlled instead of convection-controlled kinetics governs the continuous etching of aluminium yolk. The time it takes to form TiO(OH)₂ nanoshell in acid is nearly instantaneous, so practically all of our wet-processing time is spent on reaction (5), and this time duration t_{etch} is our prime optimization variable, because it controls the fill factor B in requirement (D). For near-optimal battery performance with commercial aluminium powder (diameter $D_0 \sim 50$ nm), we found that $t_{\text{etch}} = 4.5$ h gives overall the best result (discussed below), at which point we harvest the Al@TiO(OH)₂ powder by vacuum filtering.

We then calcine Al@TiO(OH)₂ powder in argon to get the final Al@TiO₂ yolk-shell (ATO) powder, during which the shell would shrink a bit. To optimize this step, TG-DSC analysis is carried out and the result is shown in Supplementary Fig. 1. The TiO(OH)₂ shell first undergoes dehydration with a weight loss of $\sim 6\%$ at a temperature of 100–300 °C. Then with continuously heating, negligible weight loss could be observed, while two exothermic peaks and one endothermic peak appear, which belong to phase transformations of amorphous TiO₂ to anatase (395 °C), anatase to rutile (560 °C) and aluminium melting (480 °C), respectively. On the basis of the TG-DSC result, the annealing temperature we used in this study is 450 °C in argon for 1.0 h, with a heating rate of 10 °C min⁻¹. This will give us anatase TiO₂ shell. Except for

the calcination, all processing steps are carried out at room temperature exposed to normal air; the entire process is industrially scalable with minimal infrastructure requirement, and the powder product is fully compatible with current slurry coating technology for battery assembly.

The interspace is adjustable through controlling the wet reaction time t_{etch} because a sufficient and well-defined internal void space is necessary to get an optimal performance of the ATO anode, as discussed in (A)-(D). To explore the critical experimental parameters, we synthesized ATO with different t_{etch} . Figure 1b and Supplementary Fig. 2a reveal the X-ray diffraction patterns of the samples with different etching time. It can be seen that the original Al₂O₃ layer is completely eliminated after our experimental procedure and the final product consists of pure aluminium and anatase, which also indicates that the outer TiO₂ was able to protect inner Al from being oxidized because we do not see any Al₂O₃ peaks (Fig. 1b). Supplementary Fig. 2b demonstrates the aluminium weight percentage for samples of different etching time determined by inductively coupled plasma analysis, and Supplementary Fig. 2c shows the corresponding specific capacity at 1C. Overall, for samples with such high aluminium percentage (85 wt %), a remarkable battery performance is observed. For $t_{\text{etch}} = 3.0$ h, the capacity is as high as 1,400 mAh g⁻¹ at 1C at 300 cycles. Severe capacity fading is observed after 300 cycles, which is believed to be due to the insufficient void space ($B \sim 2$, Supplementary Fig. 2c, red and Supplementary Fig. 11). After hundreds of cycles, the Al-Li yolk will finally rupture the TiO₂ shell. Then, repeated unstable SEI formations ensue. In contrast, for the sample with longer $t_{\text{etch}} = 4.5$ h, the initial reversible capacity is a little bit lower than the former one due to smaller yolk-to-shell weight ratio, but the performance is ultra-stable in the whole 500 cycles, illustrating the compromise between transport and mechanical considerations (A), (B), (D) in materials design. Comparing the four results, the optimal t_{etch} is determined to be 4.5 h, corresponding to $d = 30\text{--}35$ nm and $D_0 = 47$ nm (measured from transmission electron microscopy (TEM)), and $B = 2.4\text{--}3.8$.

Figure 2a shows SEM image of the as-obtained Al@TiO₂ yolk-shell particles with $t_{\text{etch}} = 4.5$ h, which clearly reveals a solid core encapsulated by a nearly spherical shell (arrows). However, it is worth mentioning that the starting aluminium nanoparticles often stick together even after sonication, and so double-yolk single-shell or even multiple-yolk single-shell structures are also obtained after reacting with acid (Supplementary Fig. 3), which does not seem to degrade the performance much. Energy-dispersive X-ray spectrum (Supplementary Fig. 4) of the nanostructure in Supplementary Fig. 3a demonstrates the presence of Al and TiO₂. TEM results indicate a complete coverage of TiO₂ (Fig. 2b), which is crucial for blocking the electrolyte convection and limiting SEI formation to the outer shell surface. Inside, aluminium nanoparticles, about $d = 30\text{--}35$ nm in diameter, are encapsulated by the TiO₂ shell, with well-defined void space in between that can accommodate the volume expansion. The TiO₂ framework, although only a few nanometres thick, was able to firmly support the core (design requirement (B)) and semi-effectively protect the chemically active aluminium (as revealed in Supplementary Fig. 5). Here we would like to reiterate the three purposes of the TiO₂ shell: first, during the acidic material preparation process, it protects the as-formed fresh aluminium particles in the core; moreover, the TiO₂ shells not only work as a conducting framework^{14,15}, but also as an electrolyte blocking layer, so SEI forms outside the shell. The element mapping in Fig. 2d–f further confirms the yolk-shell characteristic with aluminium as the core, TiO₂ as the shell and the void in between.

Half-cell battery performance of Al@TiO₂ yolk-shell nanoparticles.

The Al@TiO₂ yolk-shell nanocomposite exhibits remarkable battery performance. As shown in Fig. 3a, at a rate of 1 C, the first discharge and charge capacities are 1,237 and 1,360 mAh g⁻¹, respectively, which indicate a first-cycle CE of 90.9%. (The 9.1% unbalanced charge-discharge electrons, or ‘AWOL electrons’, in the first cycle mostly likely reflect the asymmetric formation of SEIs covering the two electrodes). Then, the specific capacity stabilizes at 1,170 mAh g⁻¹ in later cycles. Importantly, the Al@TiO₂ yolk-shell powder has long cycle life and the capacity decay is only <0.01% per cycle. The average CE is 99.2% in the

first 500 cycles. The voltage profiles for the different cycles are shown in Fig. 3b. The shape of the profile does not change from the 250th to the 500th cycle, indicating ultra-stable performance. At rate 10 C, the Al@TiO₂ yolk-shell electrode can still achieve a capacity of 661 mAh g⁻¹ after 500 cycles, twice the capacity of graphite as shown in Fig. 3c,d. We believe the excellent rate performance of ATO is due to aluminium’s good electrical conductivity, which is an advantage over Silicon as the active material. This high performance persists to 750 cycles (Supplementary Fig. 10), even though faster capacity decay ($\sim 0.03\%$ per cycle) appeared after the 500th cycle or so. Given that the SEI layer may have time-dependent growth, a slow cycling rate of 0.1 C was checked, as shown in Supplementary Fig. 8, and an even higher reversible capacity of 1,599 mAh g⁻¹ was achieved for 100 cycles.

Figure 4 shows the structure of Al@TiO₂ yolk-shell after 500 charge-discharge cycles. We see that the yolk-shell stays intact even after 500 cycles, which explains the good cyclability. The shell’s outer surface becomes thicker and rougher after the battery test, indicating the formation of the SEI layer on the TiO₂ shell. (The electrochemical stability window of the ethylene carbonate–diethyl carbonate electrolyte used in this study is 1.3–4.5 V versus Li⁺/Li, so SEI will form when the cycling voltage drops below 1.3 V.) The elemental mapping in Fig. 4d–f also reveal a perfect yolk-shell structure after 500 cycles, and therefore we can conclude that the void between the yolk and shell has successfully accommodated the volume expansion/shrinkage during the many cycles, satisfying design principles (A) and (B). We believe design principle (C) is also satisfied throughout, that is, the shell stays fully enclosed, because otherwise the SEI debris from the reactions with the electrolyte would have filled out the inside of the cavity like for other Al-based anodes²². To be able to cycle 500 times with a pristine interior surface means the shell integrity is excellent. Supplementary Fig. 9 shows the X-ray diffraction pattern of Al@TiO₂ anode at 0th, 15th and 510th cycle. Compared with the initial crystalline Al FCC structure, we see the nanoaluminum inside has turned amorphous. In (ref. 23), elemental metals tens of nanometres in domain size has turned amorphous under rapid temperature quenching. We believe electrochemical shock¹⁷ could have similar effect of solid-state amorphization²⁴.

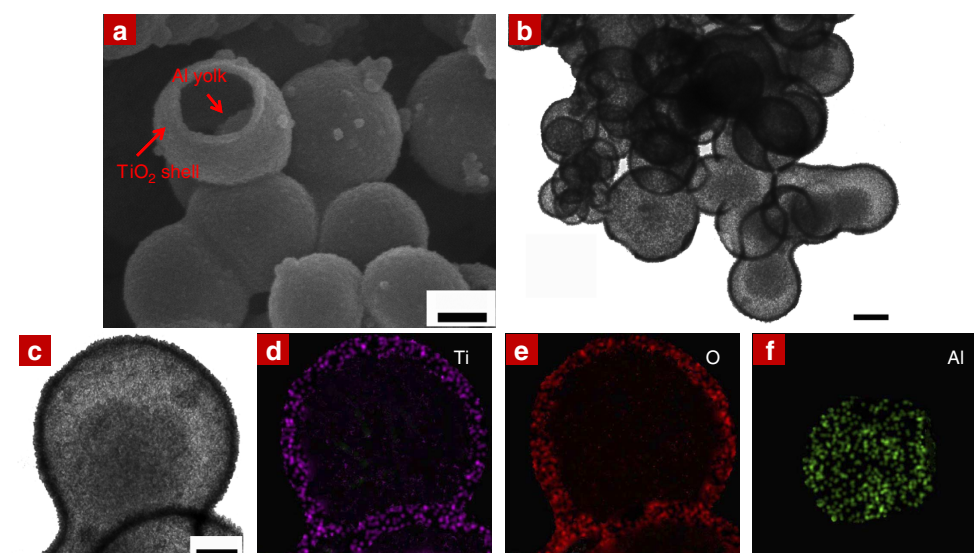


Figure 2 | Morphology analysis of the as-obtained Al@TiO₂ with etching time of 4.5 h. (a) SEM image of Al@TiO₂ with a broken shell. Bright-field transmission electron microscopy images of Al@TiO₂ at (b) low and (c) high magnifications, indicating the inner aluminium yolk encapsulated by the TiO₂ shell. Scale bars, **a** and **b**, 20 nm; **c**, 10 nm. The chemical composition was confirmed by the element mappings of (d) Ti, (e) O, and (f) Al, corresponding to the structure shown in (c).

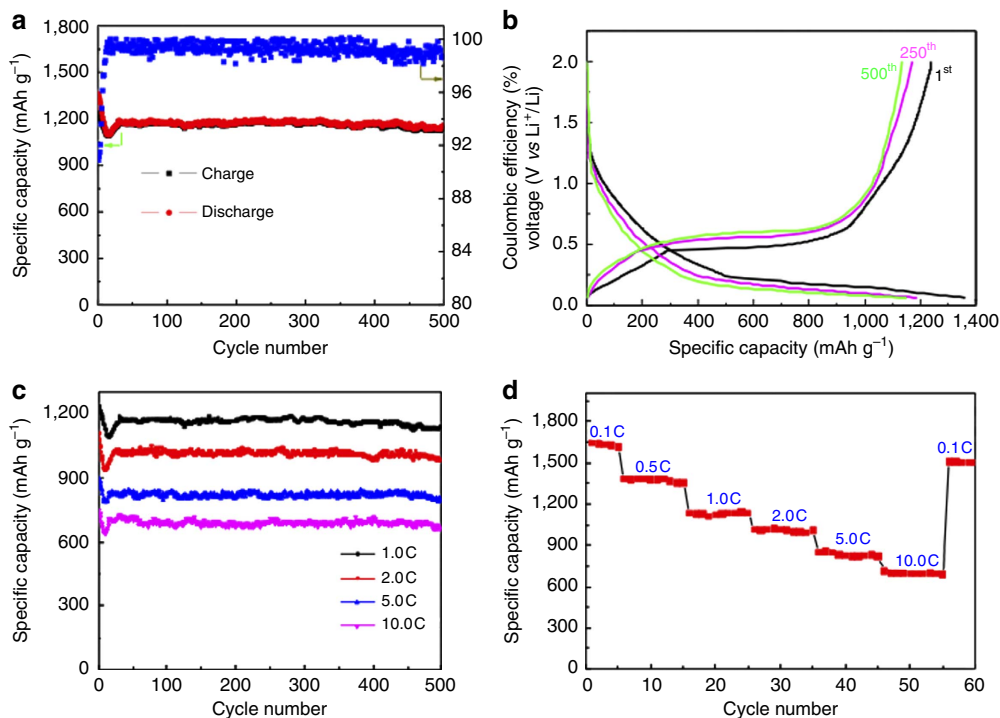


Figure 3 | Half-cell battery performance of Al@TiO₂ (4.5 h etching). (a) Cycling life and the corresponding Coulombic efficiency during 500 cycles. The charge/discharge rate was set at 1 C. (b) Charge/discharge voltage profiles with the 1st, 250th and 500th cycling. (c) Cyclability test at different charge/discharge rates. (d) Delithiation capacity evolution by varying charge/discharge rates ranging from 0.1, 0.5, 1, 2, 5, 10 C and back to 0.1 C.

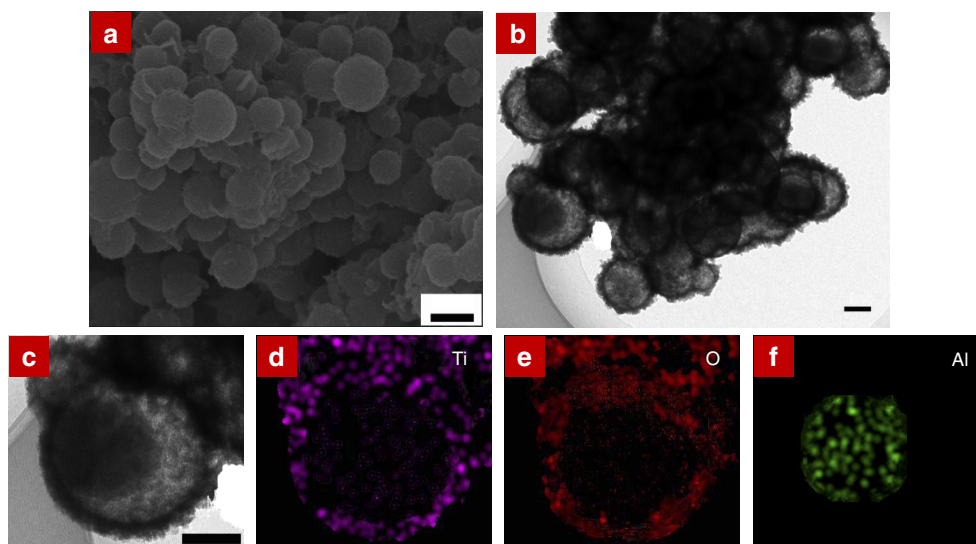


Figure 4 | Morphology evolution of Al@TiO₂ after the coin cell was tested 500 cycles. (a) a SEM and (b,c) bright-field transmission electron microscopy images of Al@TiO₂, showing the Al/TiO₂ yolk-shell structure was still well maintained after 500 cycles. Scale bars, **a** 50 nm; **b** and **c**, 20 nm. The chemical element mappings of (d) Ti, (e) O, and (f) Al, corresponding to the structure shown in (c), was confirmed by Energy-dispersive X-ray spectroscopy (EDS).

Cyclic voltammetry was performed on ATO (Supplementary Fig. 12). During the cathodic scan, the cell displayed a well-defined peak potential at 0.23 V and a prominent peak potential at 0.50 V was observed in the anodic sweep, which correspond to the discharging and charging plateau in Fig. 3b, respectively, representing the alloying/dealloying of aluminium. Meanwhile, one pair of broad cathodic/anodic peaks (located at 1.68 and 1.89 V) corresponding to Li-insertion/extraction in TiO₂ could also be detected, suggesting a pseudocapacitor-like characteristic

of TiO₂ shells during lithiation and delithiation. For the sake of comparison, completely hollow TiO₂ (without Al) was synthesized using an etching time of 24.0 h (Supplementary Fig. 6) and its cycling performance at 1 C was also characterized (Supplementary Fig. 7). The reversible capacity of hollow TiO₂ particles reaches 112 mAh g⁻¹ for the first cycle and stabilizes at 111 mAh g⁻¹ for later cycles. Moreover, it is interesting to find that the hollow TiO₂ nanoshells exhibit a quasi-linear voltage-capacity response (instead of a voltage plateau) during

galvanostatic charging-discharging, consistent with the broad cyclic voltammetry peaks at 1.68 and 1.89 V. We believe the reason for such pseudocapacitive behaviour is that when the TiO₂ shell (~3 nm) is extremely thin, a large fraction of lithium storage sites are on the surface or in near-surface regions²⁵. After deducting the TiO₂ contribution, the specific capacity with respect to nanoaluminum is calculated to be 1,246 mAh g⁻¹ at 1 C.

Full-cell performance against Li-matched LiFePO₄ cathode and Coulombic efficiency. All the tests above were performed with half-cells, where the counter-electrode used was lithium metal with super-abundant moles of lithium (~1,000%) relative to the ATO capacity. Half-cell tests are known to be unreliable checks of failure mechanism (a). Passing the more rigorous full-cell tests, where one uses lithium-molar-matched counter-electrode, would certify ATO as being close to practical use. Therefore, we have fabricated full cells with ATO anode, and LiFePO₄ (LFP) cathode with only 35% more lithium relative to the ATO capacity in half-cells. The fact that metallic lithium foil is no longer used, which served both as an abundant Li-ion source and as a reference electrode with little potential change on lithiation/delithiation, critically tests the applicability of ATO in a real-world context. Even after including all lithium ions contained in the electrolyte salt, the total lithium contained in our full cells does not exceed ~150% of the ATO capacity. Supplementary Fig. 13 shows our full cell exhibited a first discharge capacity of 1,123 mAh (g of ATO)⁻¹ at a rate of 1 C from 2.5 to 4.0 V, with a first-cycle CE = 79.4%. This means in the first cycle, >20% within the ~50% excess lithium was used to form initial SEI that cover the large surface area of Al@TiO₂ yolk-shells. This is normal and common treatment in all commercial batteries. The key question is from the second cycle on, whether the remaining <~30% excess lithium is sufficient to sustain large number of cycles. Supplementary Fig. 13 shows that it indeed does: the specific capacity stabilizes at ~968 mAh (g of ATO)⁻¹ up to 200 cycles in the full cell. This proves that the TiO₂ shells are indeed robust enough that a great majority of the Al@TiO₂ yolk-shell survives, and that the SEI is stable outside of TiO₂.

Curiously, our full-cell tests showed an average CE of only 99.48% from the 2nd to 200th cycles. Even though our ATO's CEs in half-cell and full-cell tests are actually very good compared with most of the high-capacity electrodes in the literature, it seems to violate a commonly held belief of the battery industry that the Coulombic efficiency needs to exceed 99.9% to be able to cycle 200 times, since $(0.999)^{200} = 0.82$, and 80% capacity retention is a typical definition of battery life. Our full-cell tests prove that the Coulombic efficiency does not have to be >99.9% in order for lithium-matched full cells to cycle 200 times. We believe this is because the unbalanced charge-discharge electrons (AWOL electrons) do not all tie down Lithium irreversibly. Here we believe the 0.52% absence without leave (AWOL) electrons are not all generating irreversible SEI, but instead forming reversible redox shuttle inside the electrolyte, as illustrated in Supplementary Fig. 14 (ref. 26). This is probably water-related, since it is hard to make our ATO completely dry, and a possible chemical mechanism involving hydrogen radical transport is proposed in Supplementary Note. To double check, we directly estimated the total mass of SEI on ATO by measuring the mass of ATO based anode after 50, 100, 150 and 200 cycles. There is only ~40% mass increase relative to the initial ATO weight (without binder and carbon black) after 200 full-cell cycling, shown in Supplementary Fig. 15, which is much better than previous Al-based anodes, where the SEI debris is seen to completely bury the Al²². If the AWOL electrons indeed were all used to form SEI or other irreversible products that tie down Li irreversibly and forever, then there is no way that 85.3% capacity

retention was maintained in this lithium-matched full cell after 200 cycles, since $0.52\% \times 200 > 100\%$, and utter lithium exhaustion is predicted.

We contrast ATO with existing anode technologies. Compared with metallic lithium, ATO does not form dendrites at high rate and is less of a safety concern because of air stability. Compared with Si yolk-carbon shell⁷, ATO has ~20% lower capacity below 1 C rate, but provides higher capacity with long cycle life above 1 C. Compared with high-rate Li₄Ti₅O₁₂ anode which has extremely long cycle life, ATO has 8 × gravimetric capacity at 1 C, and much better (lower) voltage. Compared with conventional graphite anode (theoretical capacity 372 mAh g⁻¹) used in current batteries, ATO has similar voltage characteristics, but has 4 × gravimetric capacity at 1 C charge/discharge rate. The fact that ATO achieves 10 C charge/discharge rate with reversible capacity exceeding 650 mAh g⁻¹ even after 500 cycles makes it a high-rate and ultrahigh-capacity anode, at an industrially satisfactory loading of 3 mg cm⁻². Simple and scalable nanostructuring has thus realized the intrinsic potential of this abundant element for battery anode.

Discussion

In summary, we developed a scalable, low-cost synthesis of Al/TiO₂ yolk-shell nano-architecture (ATO) using a wet-chemical method. The nano-scaled framework is composed of a solid Al core with an adjustable interspace, and a titanium oxide layer, which can suppress Al oxidation but not impairing electrochemical activity. The assembled half-cell using Nano-ATO as anode exhibited a long cycle life and an admirable rate capability. A largely improved capacity of ~1,200 mAh g⁻¹ along with an average CE of ~99.2% over 500 cycles at 1 C was achieved. Moreover, owing to the high Li⁺/electron conductivity of Al and TiO₂, a capacity of 661 mAh g⁻¹ still remained after 500 cycles at a fast rate of 10 C. Full-cell tests against LFP cathode with only 35% excess Lithium were successful for 200 cycles, verifying that ATO is close to real applications, as anode for high energy- and power-density Li-ion batteries.

Methods

Synthesis of Al@TiO₂ nanoparticles. Al@TiO₂ was synthesized using an 'in situ water-shift' method (See Full Method in Supplementary Methods). Specifically, 0.05 g TiOSO₄ (reagent grade, Sigma-Aldrich) and 3.0 g H₂SO₄ (ACS grade, 1.0 N, VWR) were dissolved in 100 ml deionized water. Then, 0.135 g Al powder (~50 nm in diameter, 99.9%, US Research Nanomaterials, Inc.) was added to the saturated TiOSO₄ solution. After the 30 min vigorous agitation using an ultrasound cleaner (Symphony, VMR), the solution was stirred for 3.0–10.0 h until the colour changed from grey to light. Then the resultant solution was filtrated in a vacuum system and washed three times by ethanol. After drying at 70 °C for 7.0 h in a vacuum oven (Symphony, VMR), the sample was annealed at 450 °C for 1.0 h in an Ar filled quartz tube furnace (Lindberg Blue M, Thermo Scientific). Finally, the sample was collected for the characterization and battery test.

Characterization. X-ray diffraction measurements were carried out via a Bruker D8-Advance diffractometer using Ni filtered Cu K α radiation. SEM images were collected on a FEI Sirion scanning electron microscope and TEM images were taken on a JEOL JEM-2010 transmission electron microscope operated at 200 kV. TG-DSC analysis was performed using Netzsch STA 449 with air flow at a heating rate of 10 °C min⁻¹ from room temperature to 600 °C. Inductively coupled plasma mass spectrometry was carried out using a Thermo Scientific ICAP 6300 Duo View Spectrometer. (See details in Supplementary Methods).

Electrochemical test. The battery performance of Al@TiO₂ as anode was measured using a coin cell (CR2032, Panasonic). The ATO electrode was prepared by mixing the Al@TiO₂ (70 wt %), 15 wt % conductive carbon black (Super C65, Timcal) and 15 wt % poly(vinylidene fluoride) binder (Sigma-Aldrich) in N-methyl-2-pyrrolidinone solvent (Sigma-Aldrich). The obtained slurry was coated on copper foil with a loading of 3 mg cm⁻² of Al@TiO₂ and dried at 65 °C for 24.0 h. The half-coin cell using a Li foil as a counter and reference electrode was assembled in a glove box (Labmaster sp, MBraun) filled with argon. To suppress lithium dendrite formation and also improve the cycle performance of the lithium

foil in half-cell, a Li_3N passivation layer was coated on the lithium foil electrode before battery assembly. The pretreatment procedure exposes one face of a fresh Li foil (thickness $\sim 600\ \mu\text{m}$) to flowing N_2 gas at a constant velocity for 2 h at room temperature to form Li_3N . When preparing the half-cell, the pretreated side of lithium foil would be in contact with the electrolyte. A hydraulic crimping machine (MSK-110, MTT) was used to close the cell. The electrolyte was 1.0 M LiPF_6 dissolved in 1:1 (volume) ethylene carbonate and diethyl carbonate, and a microporous polyethylene film (Celgard 2400) as the separator. The assembled cell was cycled between 0.06 to 2.0 V at various rates ranging from 0.1 to 10 C by a LAND 2001 CT battery tester. All of the specific capacities were calculated on the basis of total mass of Al@TiO_2 except the data in Supplementary Table 1 and Supplementary Fig. 10b were based on pure aluminium. The C rate was calculated on the basis of theoretical capacity $1,410\ \text{mAh g}^{-1}$ of Li_3Al_2 . The cyclic voltammetry curves were obtained at room temperature using the coin cells above between 0.06 and 2 V at a scan rate of $0.1\ \text{mV s}^{-1}$. Full cells consisting of ATO as the anode, LFP as the cathode, and a 1 M LiPF_6 EC:DEC 1:1 solution as the electrolyte were fabricated and tested. The ATO anode was prepared using the same method described above and the electrode film was punched into discs with diameter of 10 mm before battery assembling in a glove box filled with argon gas. The LFP electrodes were fabricated by spreading the mixture of LFP (Pulead Technology Industry Co., Ltd.), carbon black (Super C65, Timcal) and poly(vinylidene fluoride) binder (Sigma-Aldrich) with a weight ratio of 80:10:10 on Al current collectors. The electrode was pressed under 6–10 MPa and punched into 11 mm diameter circular disks. The active material loading was $1.3\ \text{mg cm}^{-2}$ for the ATO anode and $10.5\ \text{mg cm}^{-2}$ for the LFP cathode. The mass of ATO, LFP and even the lithium salt in the electrolyte was carefully calculated/weighed, and the total lithium contained in our full cells does not exceed $\sim 150\%$ of the ATO capacity in half-cell. The matched ATO/LFP full cells were evaluated by galvanostatic cycling in a 2,032 coin-type cell at 2.5–4.0 V, 1-C rate ($1,410\ \text{mA g}^{-1}$ of ATO). The mass of SEI layers is estimated by measuring the mass of ATO active materials based anode before and after 50, 100, 150 and 200 cycles. The normalized mass of SEI is defined as the ratio of the mass gain on ATO after cycling (presumably due to SEI layers covering ATO) to the initial ATO mass loaded in the cell without SEI. Two LFP/ATO full cells were used for the average normalized mass of SEI for each cycling condition. (See details in Supplementary Methods).

References

- Gay, E. C., Vissers, D. R., Martino, F. J. & Anderson, K. E. Performance-characteristics of solid lithium-aluminum alloy electrodes. *J. Electrochem. Soc.* **123**, 1591–1596 (1976).
- Wen, C. J., Boukamp, B. A., Huggins, R. A. & Weppner, W. Thermodynamic and mass-transport properties of LiAl . *J. Electrochem. Soc.* **126**, 2258–2266 (1979).
- Nitta, N. & Yushin, G. High-capacity anode materials for lithium-ion batteries: choice of elements and structures for active particles. *Part. Part. Syst. Char.* **31**, 317–336 (2014).
- Park, J. H. *et al.* Al-C hybrid nanoclustered anodes for lithium ion batteries with high electrical capacity and cyclic stability. *Chem. Commun.* **50**, 2837–2840 (2014).
- Liu, Y. *et al.* In situ transmission electron microscopy observation of pulverization of aluminum nanowires and evolution of the thin surface Al_2O_3 layers during lithiation-delithiation cycles. *Nano. Lett.* **11**, 4188–4194 (2011).
- Goodenough, J. B. & Kim, Y. Challenges for rechargeable Li batteries. *Chem. Mat.* **22**, 587–603 (2010).
- Liu, N. *et al.* A pomegranate-inspired nanoscale design for large-volume-change lithium battery anodes. *Nat. Nanotechnol.* **9**, 187–192 (2014).
- Huang, J. Y. *et al.* In situ observation of the electrochemical lithiation of a single SnO_2 nanowire electrode. *Science* **330**, 1515–1520 (2010).
- Wu, H. *et al.* Engineering empty space between Si nanoparticles for lithium-ion battery anodes. *Nano. Lett.* **12**, 904–909 (2012).
- Chen, S. *et al.* Silicon core–hollow carbon shell nanocomposites with tunable buffer voids for high capacity anodes of lithium-ion batteries. *Phys. Chem. Chem. Phys.* **14**, 12741–12745 (2012).
- Luo, J. *et al.* Crumpled graphene-encapsulated Si nanoparticles for lithium ion battery anodes. *J. Phys. Chem. Lett.* **3**, 1824–1829 (2012).
- Liu, N. *et al.* A yolk-shell design for stabilized and scalable Li-ion battery alloy anodes. *Nano. Lett.* **12**, 3315–3321 (2012).
- Seh, Z. W. *et al.* Sulphur-TiO₂ yolk-shell nanoarchitecture with internal void space for long-cycle lithium-sulphur batteries. *Nat. Commun.* **4**, 1331 (2013).
- Sushko, M. L., Rosso, K. M. & Liu, J. Size effects on Li⁺/electron conductivity in TiO₂ nanoparticles. *J. Phys. Chem. Lett.* **1**, 1967–1972 (2010).
- Sushko, M. L., Rosso, K. M. & Liu, J. Mechanism of Li⁺/electron conductivity in rutile and anatase TiO₂ nanoparticles. *J. Phys. Chem. C* **114**, 20277–20283 (2010).
- Gao, H. J., Ji, B. H., Jager, I. L., Arzt, E. & Fratzl, P. Materials become insensitive to flaws at nanoscale: lessons from nature. *Proc. Natl Acad. Sci. USA* **100**, 5597–5600 (2003).
- Woodford, W. H., Chiang, Y. M. & Carter, W. C. "Electrochemical Shock" of intercalation electrodes: a fracture mechanics analysis. *J. Electrochem. Soc.* **157**, A1052–A1059 (2010).
- Zhu, T. & Li, J. Ultra-strength materials. *Prog. Mater. Sci.* **55**, 710–757 (2010).
- Liu, X. H. *et al.* In situ TEM experiments of electrochemical lithiation and delithiation of individual nanostructures. *Adv. Energy Mater.* **2**, 722–741 (2012).
- Park, Y. *et al.* Si-encapsulating hollow carbon electrodes via electroless etching for lithium-ion batteries. *Adv. Energy Mater.* **3**, 206–212 (2013).
- He, Y., Yu, X. Q., Wang, Y. H., Li, H. & Huang, X. J. Alumina-coated patterned amorphous silicon as the anode for a lithium-ion battery with high coulombic efficiency. *Adv. Mater.* **23**, 4938–4941 (2011).
- Au, M. *et al.* Free standing aluminum nanostructures as anodes for Li-ion rechargeable batteries. *J. Power Sources* **195**, 3333–3337 (2010).
- Zhong, L., Wang, J., Sheng, H., Zhang, Z. & Mao, S. X. Formation of monatomic metallic glasses through ultrafast liquid quenching. *Nature* **512**, 177–180 (2014).
- Limthongkul, P., Jang, Y. I., Dudney, N. J. & Chiang, Y. M. Electrochemically-driven solid-state amorphization in lithium-silicon alloys and implications for lithium storage. *Acta Mater.* **51**, 1103–1113 (2003).
- He, K. *et al.* Transitions from near-surface to interior redox upon lithiation in conversion electrode materials. *Nano. Lett.* **15**, 1437–1444 (2015).
- Zhang, L., Zhang, Z.-C. & Amine, K. in *Lithium Ion Batteries - New Developments*. (ed. Belharouak, Ilias) (InTech, 2012).

Acknowledgements

We would like to thank the gracious help of Prof. Sanjeev Mukerjee, Prof. JiTao Chen and Prof. YunHui Huang. We acknowledge the support by NSF grant DMR-1120901 and National Natural Science Foundation of China (NSFC–No.51221291 and 51172119).

Author contributions

J.L. and C.A.W. conceived the project. S.L. and J.J.N. synthesized samples and performed battery tests. S.L. and Y.C.Z. performed the characterization. All authors analyzed the data and contributed to the discussion. S.L., J.J.N. and J.L. wrote the manuscript.

Additional information

Supplementary Information accompanies this paper at <http://www.nature.com/naturecommunications>

Competing financial interests: The authors declare no competing financial interests.

Reprints and permission information is available online at <http://npg.nature.com/reprintsandpermissions/>

How to cite this article: Li, S. *et al.* High-rate aluminium yolk-shell nanoparticle anode for Li-ion battery with long cycle life and ultrahigh capacity. *Nat. Commun.* 6:7872 doi: 10.1038/ncomms8872 (2015).



This work is licensed under a Creative Commons Attribution 4.0 International License. The images or other third party material in this article are included in the article's Creative Commons license, unless indicated otherwise in the credit line; if the material is not included under the Creative Commons license, users will need to obtain permission from the license holder to reproduce the material. To view a copy of this license, visit <http://creativecommons.org/licenses/by/4.0/>

Supplementary Figures

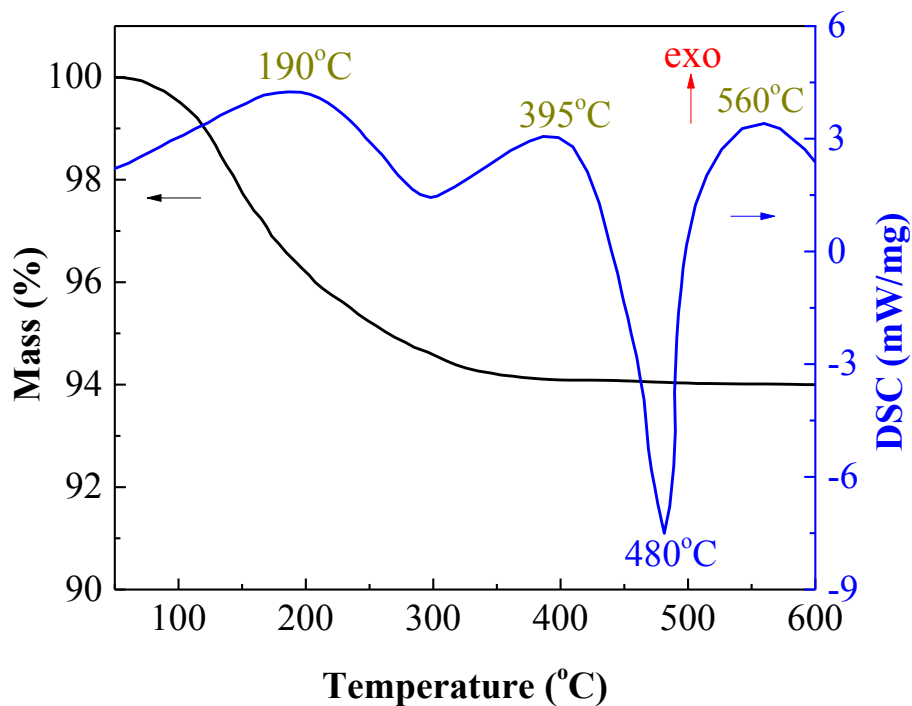


Figure 1. TG-DSC curve of the sample heated in argon from 50 to 600°C at a heating rate of 10°C/min.

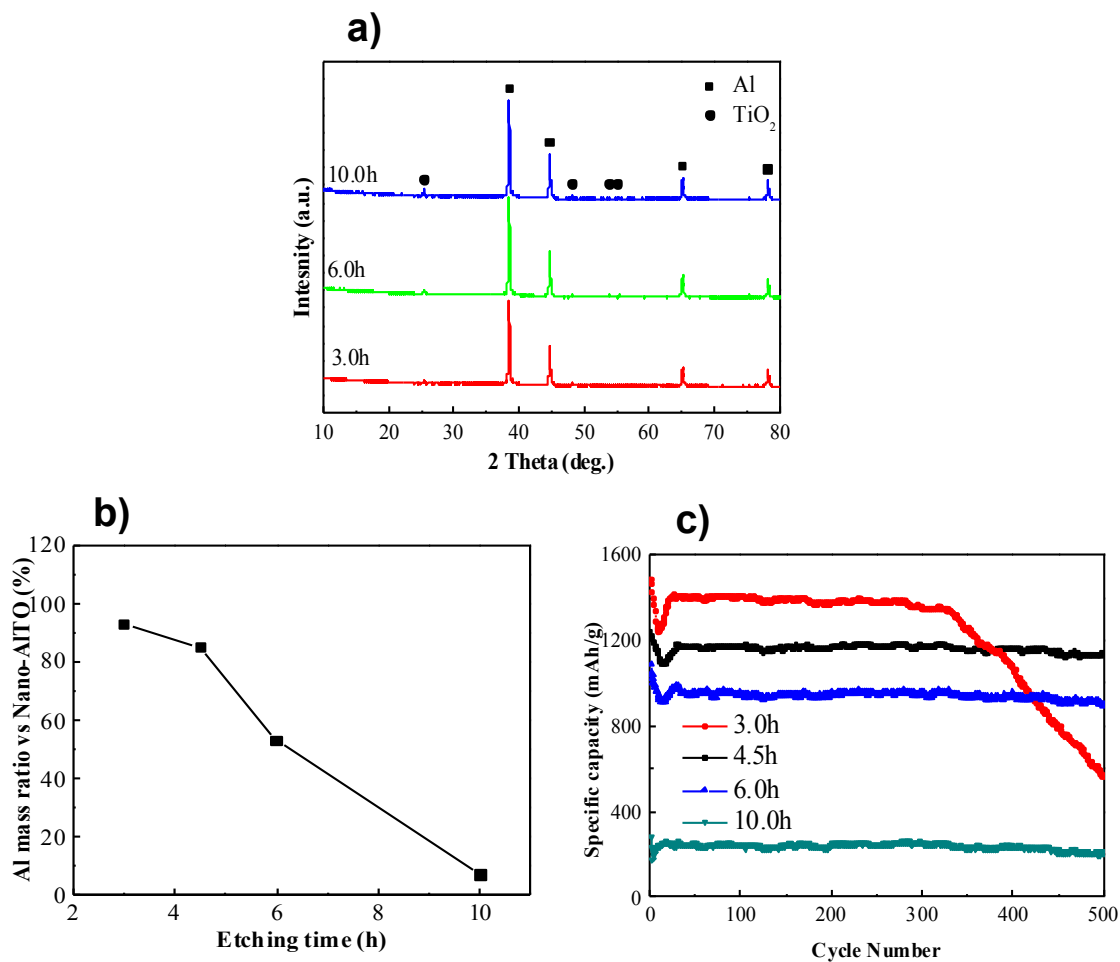


Figure 2. XRD and related battery performance of the etching time ranging 3.0 to 10.0 h. a) XRD patterns of the obtained Al@TiO₂. The crystal peaks indicate that the alumina was completely removed and a crystal TiO₂ was formed, as well as the sample with 4.5 h etching in Figure 1b. b) ICP results for Al weight ratio of samples with different etching time. c) Cycling life at 1 C. 3.0 h etching time shows rapid decay after 350 cycles since the voids are not sufficient enough.

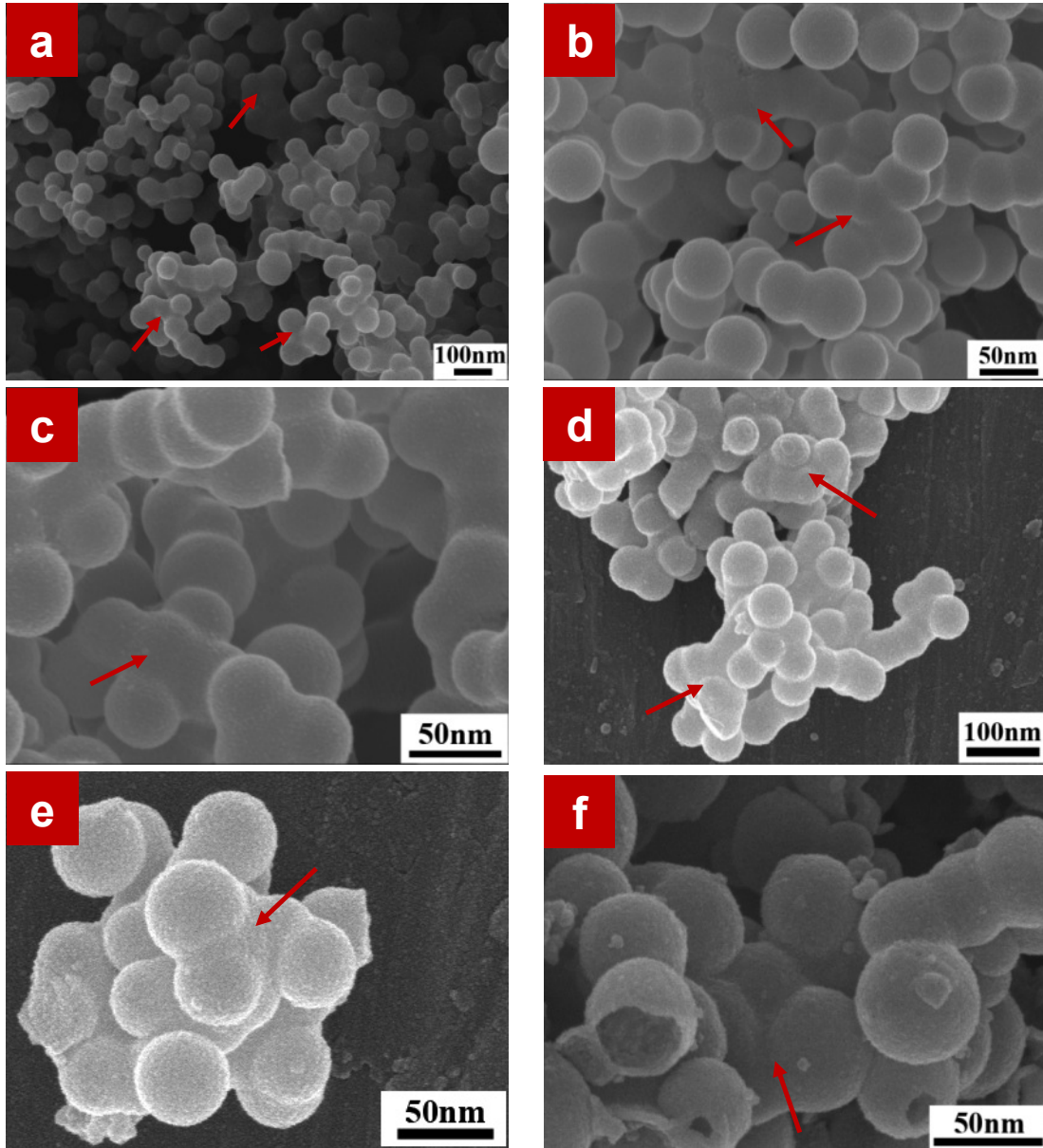


Figure 3. SEM images of as-obtained Al@TiO₂ with etching time of 4.5 h.

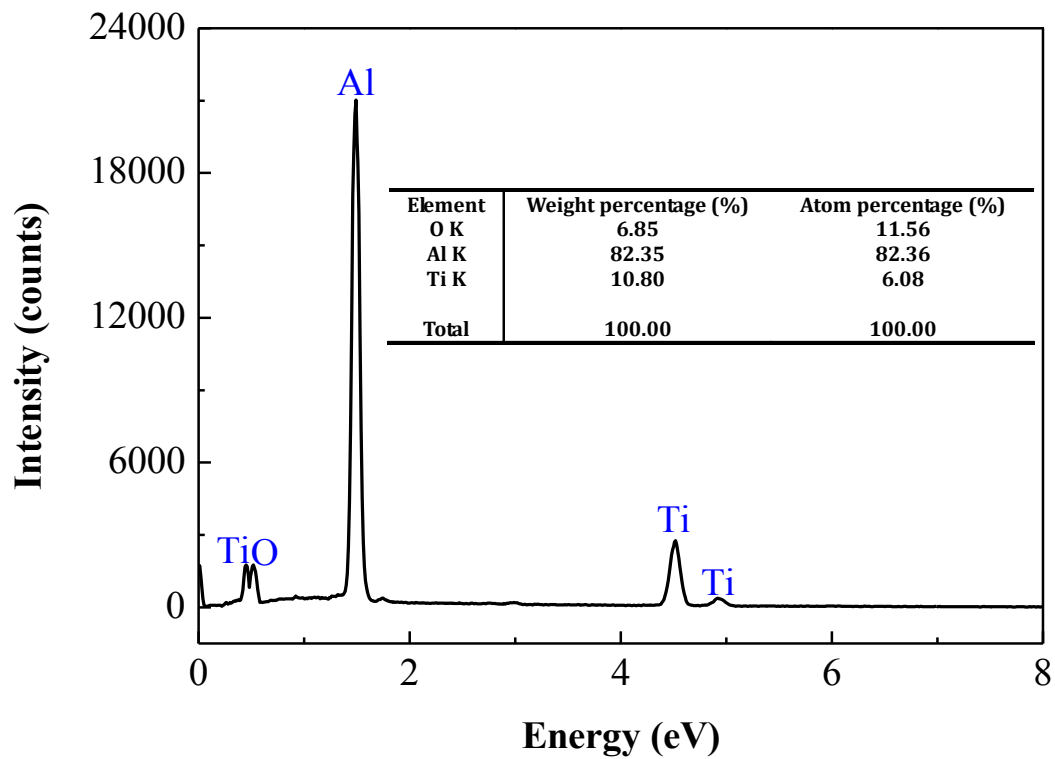


Figure 4. Energy-dispersive X-ray spectrum of the nanostructure in Figure S3a. The inset table shows that the weight fraction of Al is > 80 %.

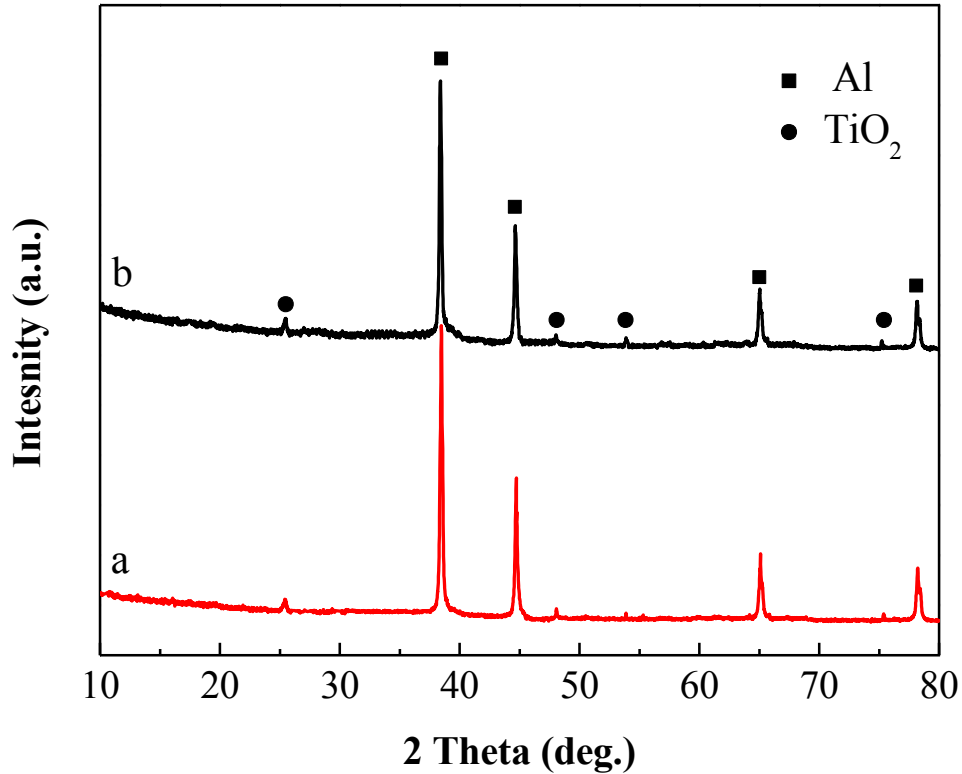


Figure 5. XRD characterization of Al@TiO₂ yolk-shell powders: a) exposed to ambient atmosphere for 24.0 h, b) grinded in air for 20 min (as we did when we prepared the electrodes, but handled without the conductive carbon black or poly(vinylidene fluoride) binder for simplicity of analysis) followed by exposing to air for another 24.0 h. No alumina peaks could be detected in both cases, which indicate negligible oxidation of aluminum core occurs.

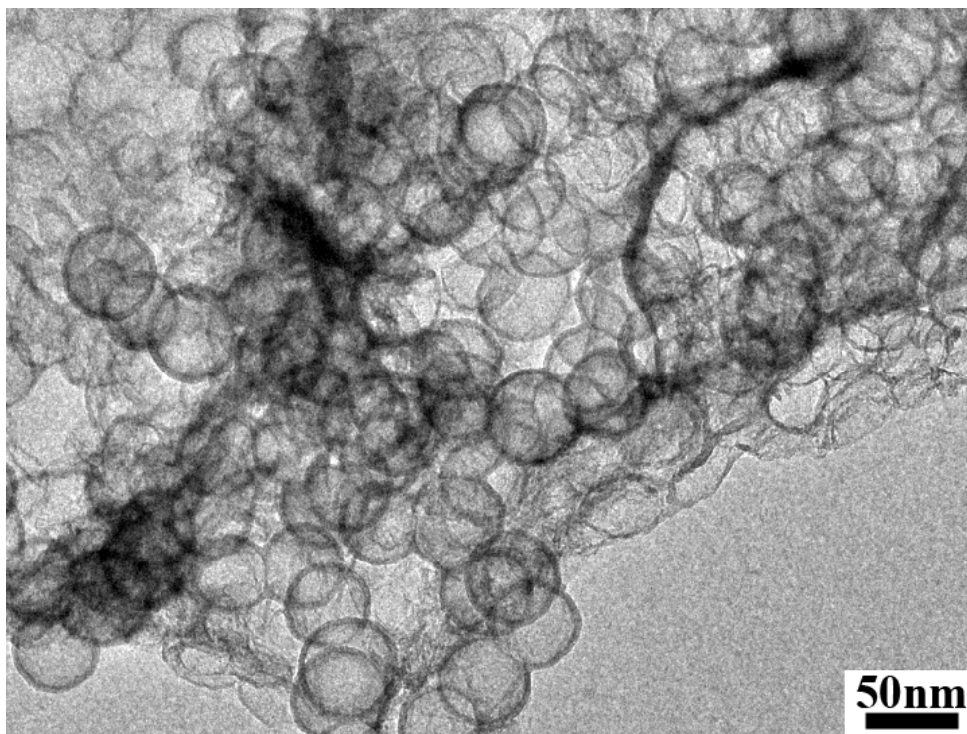


Figure 6. TEM image of the hollow TiO_2 (without Al) prepared using the etching time of **24 h**. The obvious contrast between the edge and the center also reveals its hollow nature.

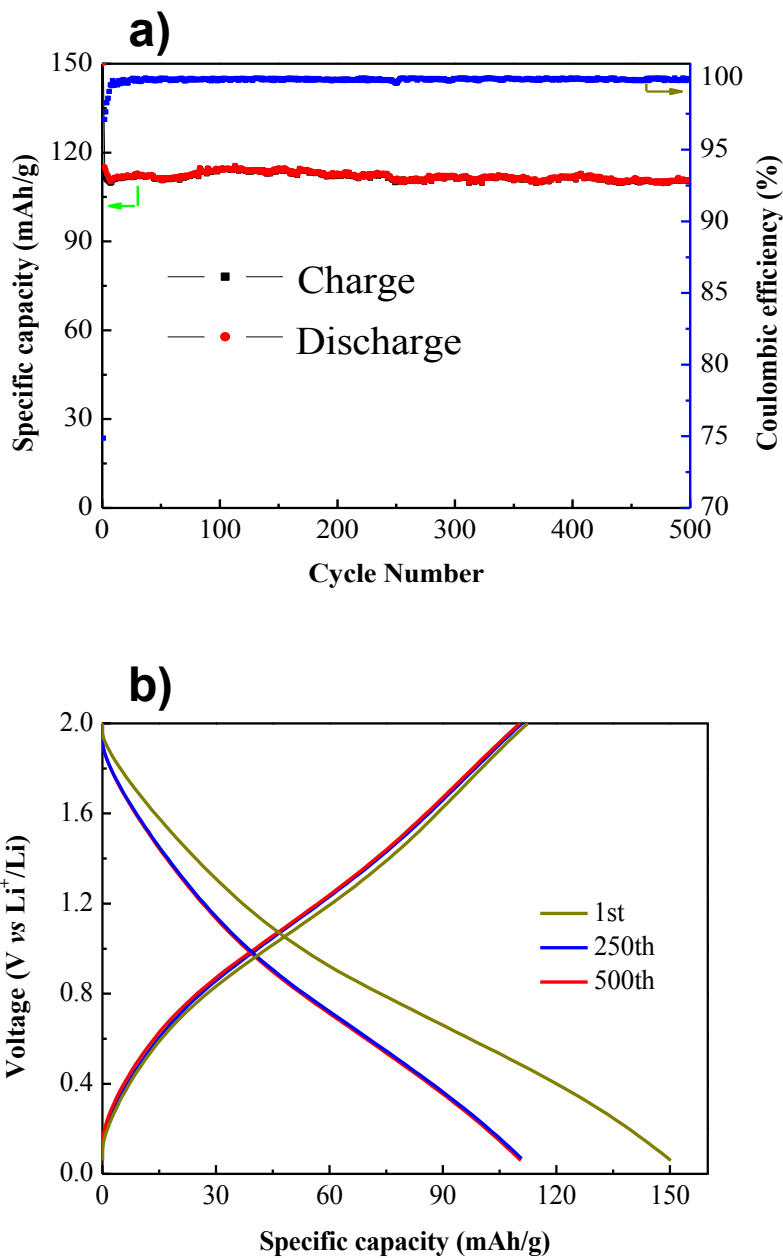


Figure 7. Battery performance of coin cells using TiO₂ hollow particles as cathode and Li foil as anode. a) Cycling life and the corresponding Coulombic efficiency during 500 cycles. The charge/discharge rate was set at 1 C. b) Charge/discharge voltage profiles with the 1st, 250th and 500th cycling.

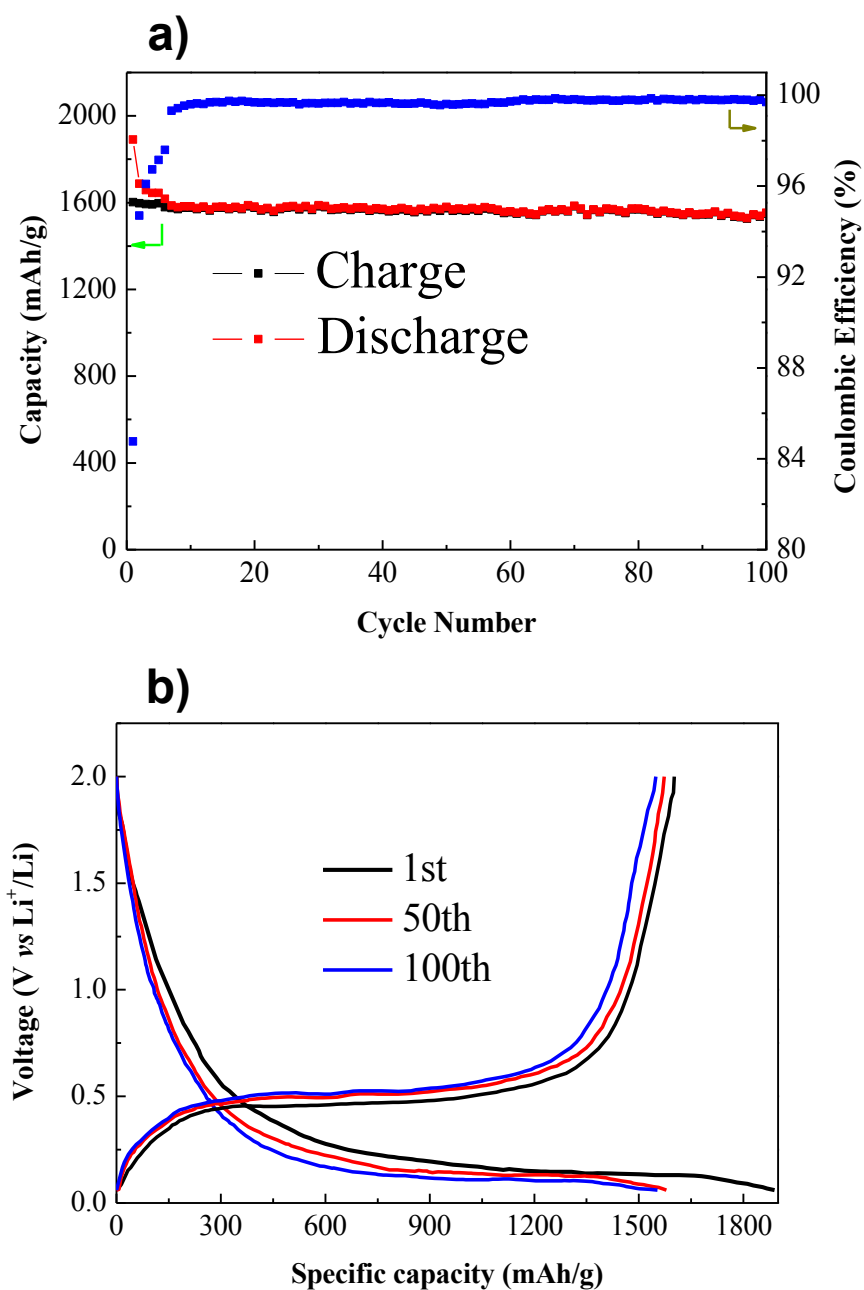


Figure 8. Battery performance of coin cells using Al@TiO₂ (4.5 h etching) as cathode and Li foil as anode. a) Cycling life and the corresponding Coulombic efficiency during 500 cycles. The charge/discharge rate was set at 0.1 C. b) Charge/discharge voltage profiles with the 1st, 50th and 100th cycling.

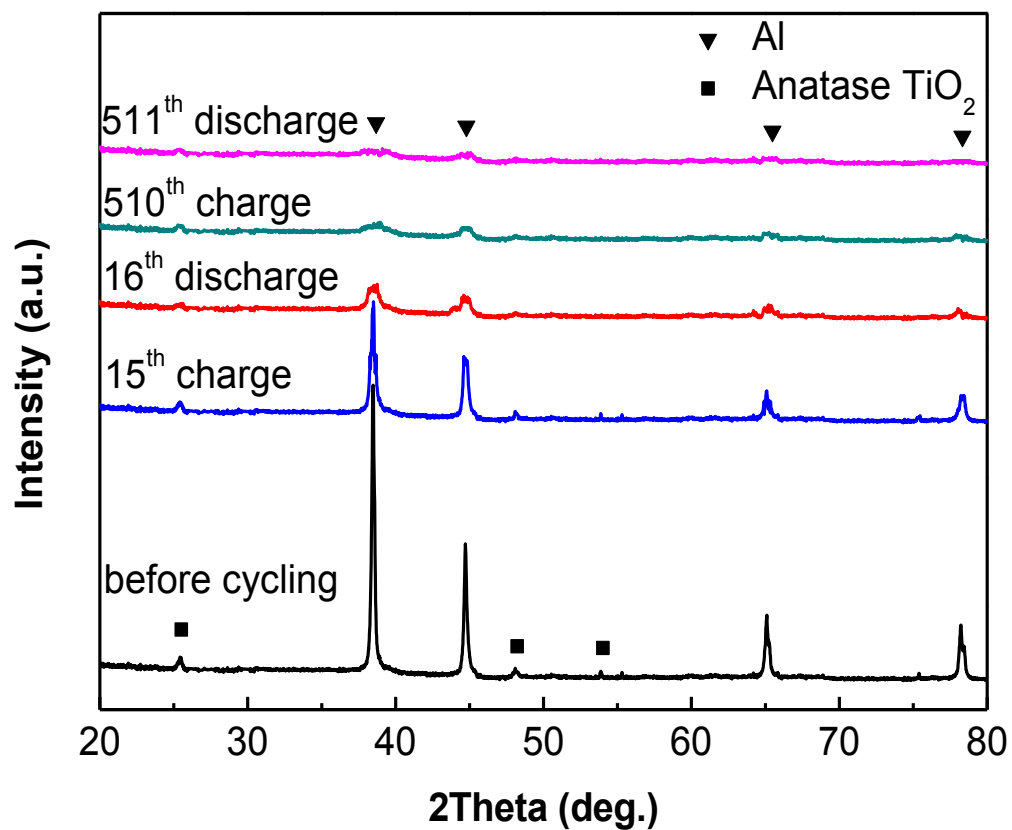


Figure 9. XRD pattern of Al@TiO₂ anode after cycling. As cycling increases, the Al FCC diffraction peaks at 38°, 44°, 65° and 78° decrease, which indicates the aluminum inside likely has turned amorphous.

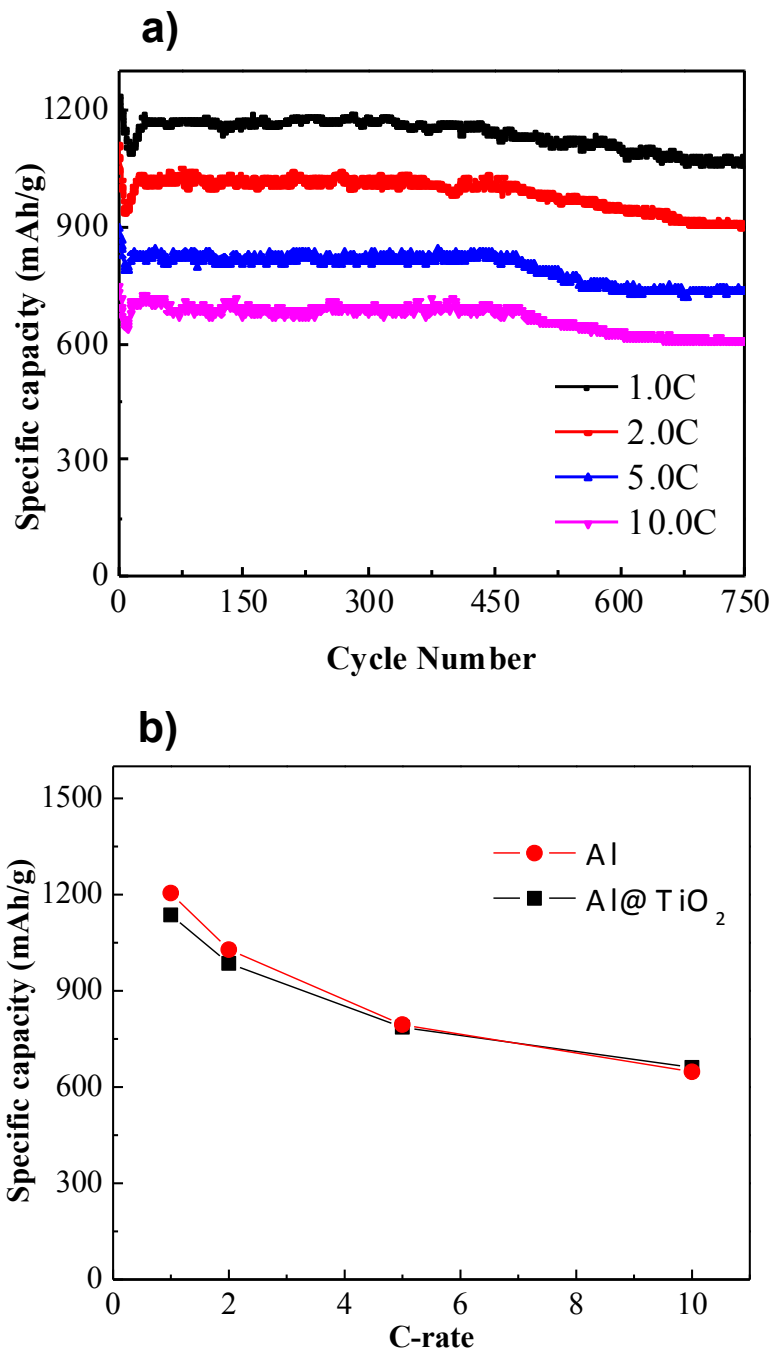


Figure 10. Battery performance of coin cells using 4.5 h etched Al@TiO₂ as anode and Li foil as cathode. a) Cyclability test at different charge/discharge rates during 750 cycles. b) The specific capacity was calculated at different charge/discharge rates according to the mass of pure aluminum.

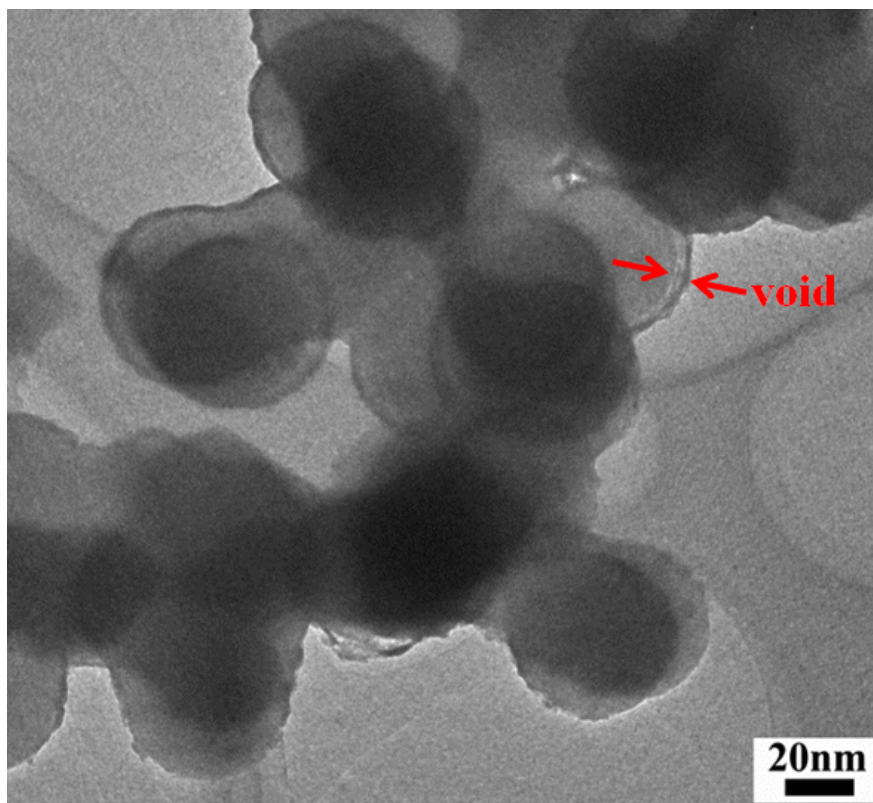


Figure 11. A TEM image of 3.0 h etched Al@TiO₂ after 450°C annealing with 1.0 h.

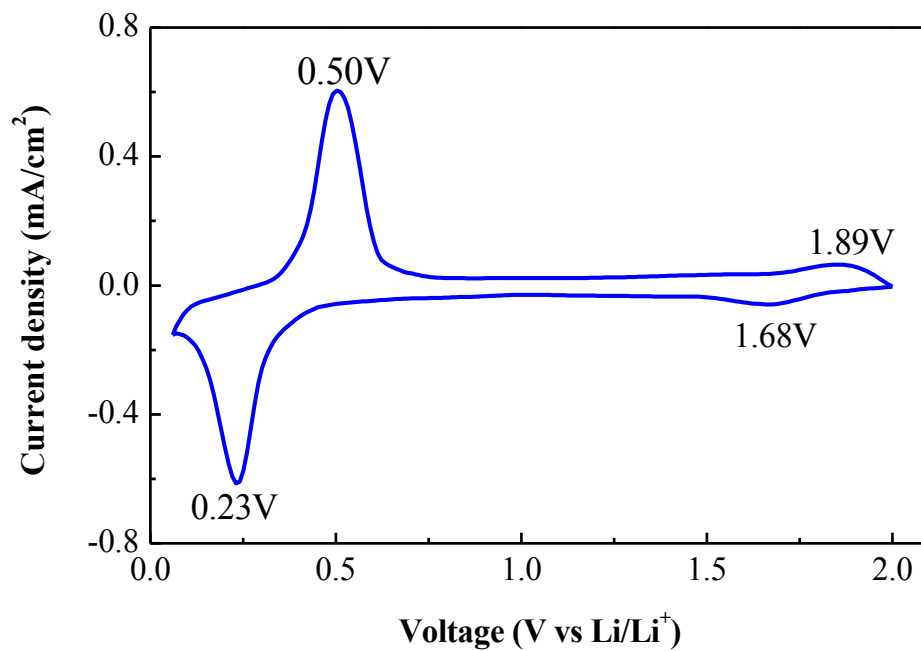


Figure 12. Cyclic voltammetry curve of an ATO/Li half-cell at 0.1 mV/s.

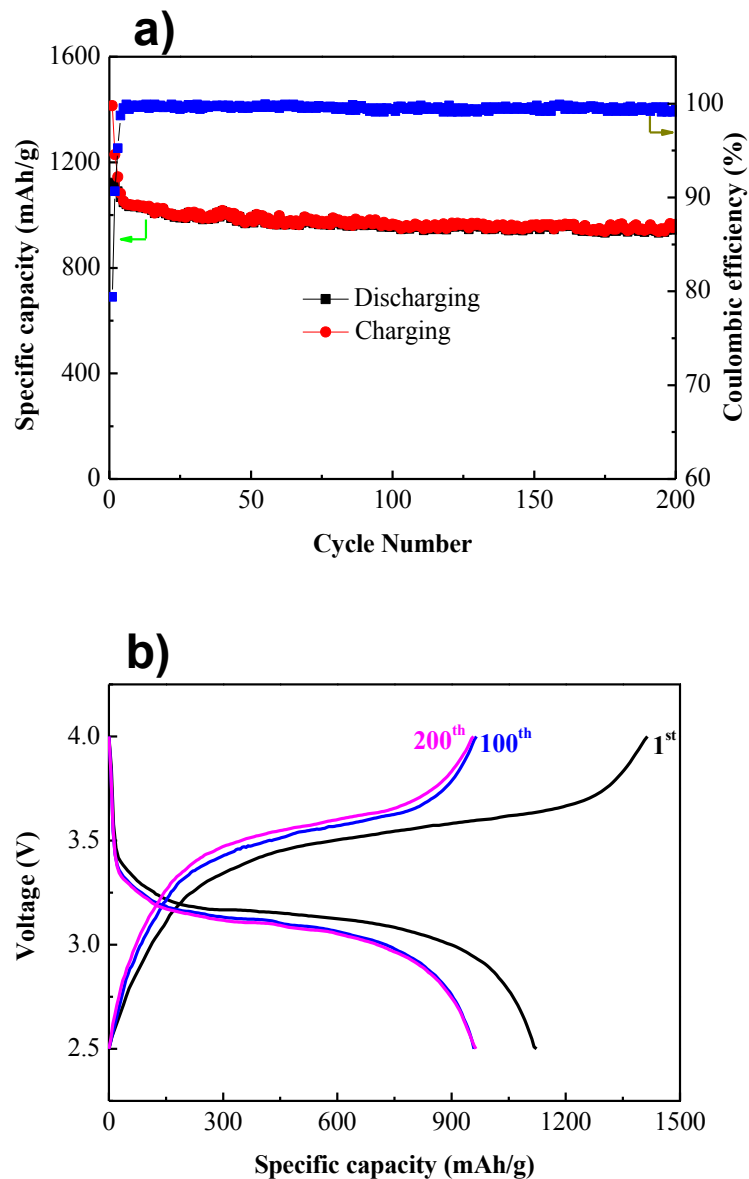


Figure 13. Battery performance of lithium-matched ATO/1M LiPF₆ EC:DEC/LFP full cells with only ~50% excess total lithium in the entire cathode and electrolyte salt compared to ATO capacity. a) Cycling life and the corresponding Coulombic efficiency during 200 cycles. The matched LFP/ATO full cells were cycled at 2.5-4.0 V, 1 C-rate (1410 mA g⁻¹ of ATO). b) Charge/discharge voltage profiles with the 1st, 100th and 200th cycling.

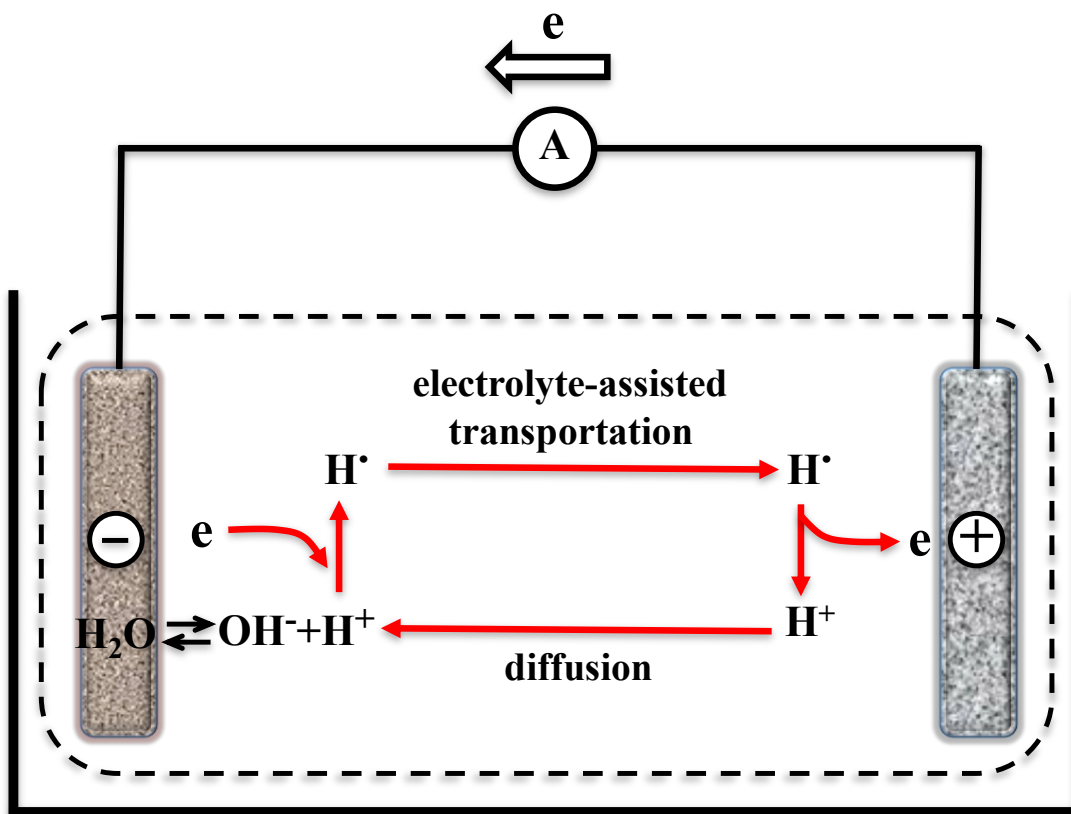


Figure 14. A possible mechanism of reversible water-related redox shuttle inside the electrolyte. (Adapted based on Fig.1 of Zhang, L., Zhang, Z.-C. & Amine, K. "Redox Shuttle Additives for Lithium-Ion Battery", in *Lithium Ion Batteries - New Developments* (ed Ilias Belharouak) (InTech, 2012).)

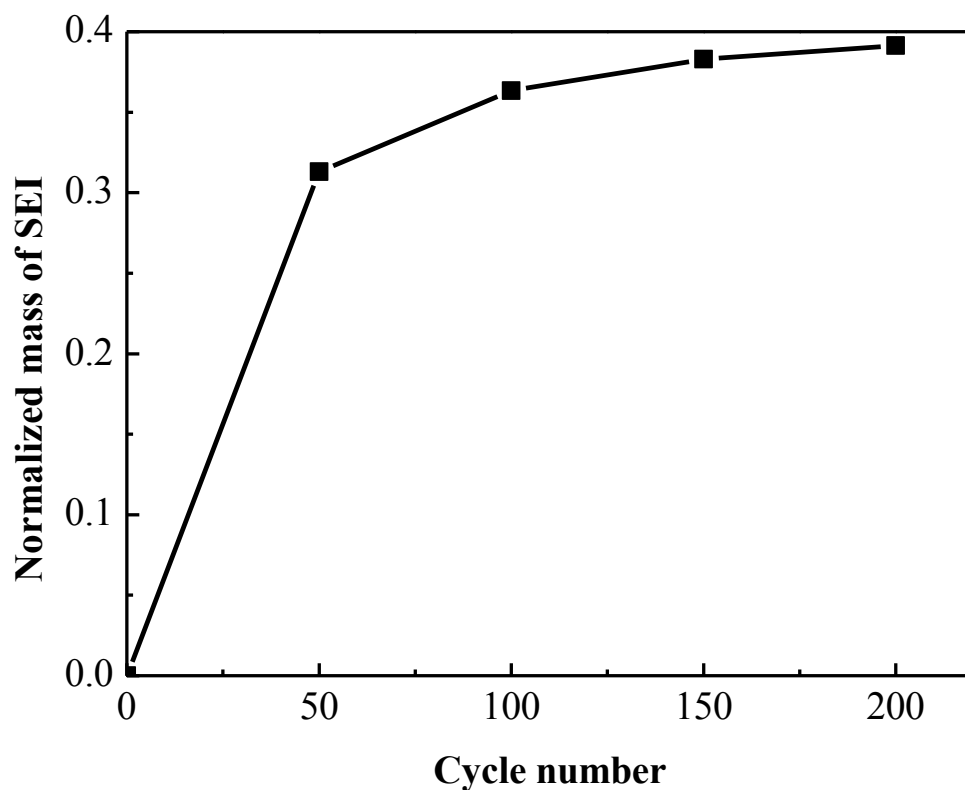


Figure 15. Mass gain of SEI on ATO in lithium-matched ATO/1M LiPF₆ EC:DEC/LFP full cells after 50, 100, 150 and 200 cycles, relative to the initial ATO weight (without binder and carbon black). Two LFP/ATO full cells were used for the average for each cycling condition.

Supplementary Table

Table 1. Comparison of battery performance of aluminum as anode in Li-ion batteries (The capacity was calculated based on the mass of aluminum).

1 st discharge capacity (mAh/g)	Reversible discharge capacity (mAh/g)	Charge/discharge rate (A/g)	Total cycle number	Degradation rate per cycle	Potential range (vs Li ⁺ /Li)	Ref.
1680	922 (100 th)	6.0	100	0.60%	0.01-3 V	1
1200	100 (10 th)	0.7	10	22.00%	0.01-3 V	2
1390	800 (1 st)	0.25	1	42.40%	0.01-1.2 V	3
977	<200 (25 th)	~1.0	25	>6.0%	0.01-1 V	4
1468	1246 (500th)	1.4	500	0.01%	0.06-2 V	Current work
	1205 (750th)	(1.0 C vs Al₂Li₃)	750	0.03%		

Supplementary Notes

To select an appropriate annealing temperature for Al@TiO₂, TG-DSC analysis was carried out, as shown in Supplementary Fig. 1. First the sample went through a dehydration process, displaying a loss of ~6 wt% at 100-300°C. Then a negligible weight loss was observed along with two exothermic and one endothermic peaks, which correspond to amorphous to anatase (395°C), anatase to rutile (560°C) TiO₂ phase transformation, and aluminum melting (480°C), respectively. For the purpose of obtaining crystal anatase TiO₂, we chose 450°C as the optimized annealing temperature in this study.

Supplementary Fig. 2a shows XRD patterns of Al@TiO₂ with etching time of 3.0, 6.0 and 10.0 h. It can be seen that the final product only consisted of pure aluminum and anatase TiO₂. Apparently the native Al₂O₃ layer was fully replaced by TiO₂ at different reaction time from 3.0 to 10.0 h. The reaction time mainly affects the size of interstitial space via dissolving the aluminum core. Supplementary Fig. 2b shows the aluminum concentration dependence on etching time. A shorter 3.0 h treatment enables a high aluminum concentration of >93 wt%, which indicates a small interspace (Supplementary Fig. 11). The interspace volume is estimated to be ~30% of the aluminum core, which is not enough to accommodate aluminum's ~96% volume expansion in lithiation. As a result, the TiO₂ shell was possibly damaged and thus a fast capacity decay happened (Supplementary Fig. 2c, red). A longer etching introduces a bigger interspace, which leads to better accommodation and then a good cyclability (Supplementary Fig. 2c). However, a lower aluminum ratio (~53 wt% with 6.0 h and ~7 wt% with 10.0 h) will introduce a lower specific capacity, which was calculated upon the total mass of Al@TiO₂ (Supplementary Fig. 2b). In parallel, larger interspace will reduce conductivity because of the loose contact, leading to higher impedance. The Al@TiO₂s treated with 6.0 and 10.0 h only show a specific capacity of ~903 and ~209 mAh/g after 500 cycles, respectively (Supplementary Fig. 2c). In conclusion, the sample of ~85 wt% Al with 4.5 h etching was selected to possess a near-optimal battery performance.

Supplementary Fig. 3 shows the double-yolk-single-shell or even multiple-yolk-single-shell structures caused by insufficient sonication and nanoparticle dispersal in acid. Energy-dispersive X-ray spectrum (Supplementary Fig. 4) of the nanostructure in Supplementary Fig. 3a demonstrates the presence of Al and TiO₂. The inset table shows that the weight fraction of Al is >80 %, which is also consistent with our ICP result in Supplementary Fig. 2b.

As we mentioned in the requirements of Al@TiO₂ yolk-shell nanostructures, the shell must be mechanically robust and fully closed. We believe our TiO₂ shell could semi-effectively protect the Al core. To verify this speculation, we did the XRD characterization of Al@TiO₂ yolk-shell powders that were exposed to ambient air for 24 h and grinded in air for 20 min (as we did when we prepared the electrodes, but handled without the conductive carbon black or poly(vinylidene fluoride) binder for simplicity of analysis) followed by exposing to air for

another 24 h. As revealed in Supplementary Fig. 5, no alumina peaks could be detected in both cases, which indicate negligible oxidation of aluminum core have occurred. Therefore, it is reasonable to conclude that Al@TiO₂ yolk-shell nanostructures are air stable for at least 24 h and the TiO₂ shell is mechanically robust to survive the mixing and handling during the electrode preparation.

The hollow TiO₂ (without Al) was obtained using an etching time of 24 h and the obvious contrast between the edge and the center in Supplementary Fig. 6 confirmed its hollow nature. The battery performance of the hollow TiO₂ shells was characterized, as shown in Supplementary Fig. 7. The reversible capacity reaches 112 mAh/g for the first cycle and stabilizes at 111 mAh/g for later cycles at a rate of 1 C. The average Coulombic efficiency is about 99.83% in the whole 500 cycles. The high reversibility also indicates the pseudocapacitive nature of the hollow TiO₂ shells.

The cycle performance at a slow rate of 0.1C was characterized for 100 cycles (Supplementary Fig. 8). The reversible capacity reaches 1638 mAh/g for the first cycle and stabilizes at 1599 mAh/g for later cycles at a rate of 0.1 C. The average Coulombic efficiency is about 99.41% in the first 100 cycles.

Supplementary Fig. 9 shows the XRD pattern of Al@TiO₂ anode after cycle. With increasing cycles, the Al FCC diffraction peaks at 38°, 44°, 65° and 78° decreases, which indicate the aluminum inside likely has turned amorphous.

In regards to aluminum as the active material, for a comparison, the specific capacity of Al@TiO₂ battery vs pure aluminum with different cycles and rates were also calculated. As shown in Supplementary Fig. 10b, the specific capacity of 1205 (1 C), 1028 (2 C), 795 (5 C), and 647 mAh/g (10 C) after 500 cycles was respectively attained, which further indicates the outstanding battery performance of the ATO electrode.

In our half-cell experiments, the average CE from 1st to 500th cycle is calculated to be 99.2%. However the 0.8% AWOL electrons are not all generating irreversible SEI, but we believe forming reversible redox shuttle inside the electrolyte, as illustrated in Supplementary Fig. 14. We have proposed it is water related. When there is a little bit of residual water in the electrode, which is reasonable in our situation considering that we prepare the electrodes in a moisture-containing environment, the redox shuttle mechanism may be activated between the Al@TiO₂ (ATO) cathode and lithium anode. During discharging, the absorbed water would firstly receive electrons ($\text{H}_2\text{O} + \text{e}^- \rightarrow \text{H}^\bullet + \text{OH}^-$), producing hydrogen radical (H[•]). Then the active hydrogen would preferably attach to the organic electrolyte, ethylene carbonate ((CH₂O)₂CO), for example, with the lone pair of the oxygen atom of carbonyl group in the EC interacting with the unsaturated hydrogen radical.



In this form, the hydrogen radical is protected from intermolecular annihilation and thus stabilized to survive the diffusion circle. Once the H^\bullet is translated to the lithium metal, it would release the electron to form H^+ again ($\text{H}^\bullet \rightarrow \text{H}^+ + \text{e}^-$), which would diffuse back to the Al@TiO₂ electrode. The “oxidation-diffusion-reduction-diffusion” cycle can be repeated continuously due to the reversible nature of the redox shuttle. We did an estimation based on the Faraday’s law. When the water fraction reaches 0.2% of the active materials, the Coulombic efficiency loss that comes from the residual water approaches 0.5%.

Supplementary Methods

Synthesis of Al@TiO₂ nanoparticles

Large quantities of Al@TiO₂ composites were synthesized through an “*in situ* water-shift” strategy (Figure 1a). In a typical experiment, we first prepare saturated titanium oxysulfate solution with 0.05 g TiOSO₄ (reagent grade, Sigma-Aldrich) and 3.0 g H₂SO₄ (ACS, 1N, VWR) dissolved in 100 mL DI water. Then 0.135 g commercial aluminum powders (99.9%, US Research Nanomaterials, Inc.), which showed an average diameter of ~50 nm in TEM images, were added to the saturated titanium oxysulfate solution. Then the mixture was sonicated with 30 min using an ultrasound cleaner (SymphonyTM, VMR). The obtained slurry was continuously stirred with 3.0-10.0 h afterwards until the color changed from grey to light. The resultant solution under different reaction time was then filtrated in a vacuum system and washed three times by ethanol. The received paste was dried at 70°C with 7.0 h in a vacuum oven (SymphonyTM, VMR). The dried sample was annealed at 450°C with 1.0 h in an Ar filled quartz tube furnace (Lindberg Blue M, Thermo Scientific). After cooling to room temperature, the sample was collected for the following characterization and battery test.

Characterization

XRD measurements were carried out via a Bruker D8-Advance diffractometer using Ni filtered Cu K α radiation. The applied current and voltage were 40 mA and 40 kV, respectively. During the analysis, the sample was scanned from 10 to 70° at a speed of 4°/min. SEM images were collected on a FEI Sirion scanning electron microscope (accelerating voltage 5 kV) equipped with energy-dispersive X-ray spectroscopy and TEM images were taken on a JEOL JEM-2010 transmission electron microscope operated at 200 kV. TG-DSC analysis was performed using Netzsch STA 449 with air flow at a heating rate of 10°C/min from room temperature to 600°C. Inductively coupled plasma mass spectrometry (ICP-MS) was carried out using a Thermo Scientific ICAP 6300 Duo View Spectrometer.

To characterize the anode morphology evolution after cycling (Figure 4), the coin cell was opened after 500 cycles. The Al@TiO₂ anode was washed in acetonitrile to remove the electrolyte and rinsed with ethanol 3 times.

Electrochemical Test

The battery performance of Al@TiO₂ as anode was tested using a coin cell (CR2032, Panasonic). The working electrode was prepared by mixing Al@TiO₂ (70 wt%) with 15 wt% conductive carbon black (Super C65, Timcal), and 15 wt% poly(vinylidene fluoride) binder (average M_n ~71,000, Sigma-Aldrich) in N-methyl-2-pyrrolidinone (NMP, Sigma-Aldrich), which then was coated onto a copper foil with a loading of 3 mg/cm² of the Al@TiO₂ and dried at 65°C for 24.0 h in an oven (SymphonyTM, VMR). The coin cell using a lithium foil as counter electrode was assembled in a glove box (Labmaster sp, MBraun) filled with argon (both O₂ and

H₂O <0.1 ppm). To suppress lithium dendrite formation and also improve the cycle performance of the lithium foil in half-cell, a Li₃N passivation layer was coated on the lithium foil electrode before battery assembly. The pretreatment procedure exposes one face of a fresh Li foil (thickness ~600 μm) to flowing N₂ gas at a constant velocity for 2 h at room temperature to form Li₃N. When preparing the half-cell, the pretreated side of lithium foil would be in contact with the electrolyte. A hydraulic crimping machine (MSK-110, MTI) was used to pack the cell. The electrolyte was 1.0 M LiPF₆ dissolved in 1:1 volume ratio ethylene carbonate and diethyl carbonate, and a microporous polyethylene film (Celgard 2400) as the separator. Before use, the separator was soaked in the electrolyte overnight. The assembled cell was cycled in the fixed voltage window between 0.06 to 2.0 V at various rates ranging 0.1 to 10 C with an LAND 2001 CT battery tester. All of the specific capacities were calculated on the basis of the total mass of Al@TiO₂ except the data in Table S1 and Figure S6 were based on pure aluminum. The cyclic voltammetry curves were obtained at room temperature using the coin cells above between 0.06 and 2 V at a scan rate of 0.1 mV/s. Full cells consisting of ATO as the anode, LiFePO₄ (LFP) as the cathode, and a 1M LiPF₆ EC:DEC 1:1 solution as the electrolyte were fabricated and tested. The ATO anode was prepared using the same method described above and the electrode film was punched into discs with diameters of 10 mm before battery assembling in a glove box filled with argon gas. The LFP electrodes were fabricated by spreading the mixture of LFP (Pulead Technology Industry Co., Ltd.), carbon black (Super C65, Timcal) and poly(vinylidene fluoride) binder (Sigma-Aldrich) with a weight ratio of 80:10:10 onto Al current collectors. The electrode was pressed under 6-10 MPa and punched into 11 mm diameter circular disks. The active material loading was 1.3 mg/cm² for the ATO anode and 10.5 mg/cm² for the LFP cathode. The mass of ATO, LFP and even the Lithium salt in the electrolyte was carefully calculated/weighed, and the total lithium contained in our full cells does not exceed ~150% of the ATO capacity in half-cell. The matched ATO/LFP full cells were evaluated by galvanostatic cycling in a 2032 coin-type cell at 2.5-4.0 V, 1 C-rate (1410 mA g⁻¹ of ATO). The mass of SEI layers is estimated by measuring the mass of ATO active materials based anode before and after 50, 100, 150 and 200 cycles. The normalized mass of SEI is defined as the ratio of the mass gain on ATO after cycling (presumably due to SEI layers covering ATO) to the initial ATO mass loaded in the cell without SEI. Two LFP/ATO full cells were used for the average normalized mass of SEI for each cycling condition.

Supplementary References

- 1 Park J H, Hudaya C, Kim A Y, et al. Al–C hybrid nanoclustered anodes for lithium ion batteries with high electrical capacity and cyclic stability. *Chem Commun* **50**, 2837-2840, (2014).
- 2 Au M, McWhorter S, Ajo H, et al. Free standing aluminum nanostructures as anodes for Li-ion rechargeable batteries. *J Power Sources* **195**, 3333-3337, (2010).
- 3 Hamon Y, Brousse T, Jousse F, et al. Aluminum negative electrode in lithium ion batteries. *J Power Sources* **97-8**, 185-187, (2001).
- 4 Hudak N, Huber D. Nanostructured Lithium-Aluminum Alloy Electrodes for Lithium-Ion Batteries. *ECS Transaction* **33**, 1-13 (2011)